

Article

Design Optimization and Coupled Dynamics Analysis of an Offshore Wind Turbine with a Single Swivel Connected Tether

Jieyan Chen ¹ and Chengxi Li ^{2,*} 

¹ Department of Ocean Engineering, Texas A&M University, College Station, TX 77084, USA; jieyan@tamu.edu

² Department of Mechanical Engineering, Massachusetts Institute of Technology, Cambridge, MA 02139, USA

* Correspondence: chengxi@mit.edu

Received: 18 May 2020; Accepted: 7 July 2020; Published: 8 July 2020



Abstract: The increased interest in renewable wind energy has stimulated many offshore wind turbine concepts. This paper presents a design optimization and a coupled dynamics analysis of a platform with a single tether anchored to the seabed supported for a 5 MW baseline wind turbine. The design is based on a concept named SWAY. We conduct a parametric optimization process that accounts for important design considerations in the static and dynamic view, such as the stability, natural frequency, performance requirements, and cost feasibility. Through these optimization processes, we obtain and present the optimized model. We then establish the fully coupled aero-hydro-servo-elastic model by the time-domain simulation tool FAST (Fatigue, Aerodynamics, Structures, and Turbulence) with the hydrodynamic coefficients from an indoor program HydroGen. We conduct extensive time-domain simulations with various wind and wave conditions to explore the effects of wind speed and wave significant height on the dynamic performance of the optimized SWAY model in various water depths. The swivel connection between the platform and tether is the most special design for the SWAY model. Thus, we compare the performance of models with different tether connection designs, based on the platform motions, nacelle velocity, nacelle accelerations, resonant behaviors, and the damping of the coupled systems. The results of these comparisons demonstrate the advantage of the optimized SWAY model with the swivel connection. From these analyses, we prove that the optimized SWAY model is a good candidate for deep water deployment.

Keywords: renewable energy; offshore wind turbine; design optimization; coupled dynamics analysis

1. Introduction

Nonrenewable energy resources, such as coal, natural gas, and oil, are primary sources of energy. However, these fossil fuels continue to be depleted, and are harmful to the environment. Therefore, vast wind resources have received much attention because of their excellent potential for electricity generation. Moreover, since wind energy is green and inexhaustible, it reduces the world's dependency on fossil fuels. Among the different kinds of wind turbines, oceanic floating offshore wind turbines (FOWT) are an excellent solution to avoid interference with life on the land and achieve higher energy efficiency due to the steadier and higher annual mean offshore wind velocity. There have been many theoretical and conceptual studies on FOWT [1–3]. A typical FOWT is composed of an upper structure containing the wind turbine rotor supported by a tower and the lower support platform below the mean water level. Different types of upper wind turbine models have been proposed and used in many studies, such as the National Renewable Energy Laboratory (NREL) 10-MW wind turbine [4–6] and NREL 5-MW wind turbine [7–10]. In the present study, we use the NREL 5 MW baseline wind turbine, a design derived from onshore wind turbines under the standards IEC 61400-3 [11]. Combining the

mechanism of operating machines and theoretical designs, this configuration is the realization of a three-bladed upwind floating wind turbine with a 5-MW power capacity.

For the other part of the FOWT, the supported platform involves more complex hydrodynamics and fluid-structure interactions. Researchers have proposed several types of floating supported platforms throughout the years. One example is the Hywind FOWT, which contains a spar-buoy with catenary mooring systems [12] to support the large-scale NREL 5 MW reference wind turbine. Additionally, the 5 MW wind turbine tower and control system is modified to allow coupling and to ensure positive aerodynamic damping during operation. Similar numerical and experimental studies for FOWTs with the spar-type platforms have been proposed and carried out throughout the year [13–15]. Another possible candidate for the FOWT support platform is the distributed-buoyancy stabilization (barge) [16–18]. It achieves excellent stability with a high-water plane area, and its mooring system is primarily for station keeping and not for supplying the system stiffness. The tensioned leg platform (TLP-type) support platform is another favorite choice for the FOWT. This concept is promising in intermediate water depths, because it has limited platform motion. Several studies use coupled dynamics analysis to analyze the TLP dynamic performance and the corresponding tension loads [19–22]. Numerical optimization for the design of TLP-type FOWT has also been carried out in many studies [23–27]. Other types of support platforms, such as semi-submersible platforms, are also employed for offshore wind turbine support. The main feature of the semi-submersible concept is that its main structures are located deep below the water surface to reduce wave load and global motion, which makes this structure ideal for supporting a large offshore wind turbine. The designs, such as the WindFloat design [28], DeepCWind [29], and HiPR Wind [30], are all examples of semi-submersible concepts. One of the latest concepts of the support platform is SWAY[®] [31], an advanced realization for FOWTs. The patented SWAY system consists of a floating tower that extends deep into the water, and a single pipe that is anchored to the seabed and connected to the platform with a swivel connection at the fairlead (see Figure 5 of [31]). With a floating ballast pole at the lower end, the center of gravity (CG) of the tower is much lower than the center of buoyancy (CB), which helps to achieve stability. The rotor is downwind orientated with three blades. When the wind hits the structure, the entire tower rotates via the subsea swivel, reinforcing the alignment of the tower with the wind. These properties improve energy efficiency and make it possible to add wire bracing to the tower, to enhance stiffness for carrying larger turbines.

As the SWAY concept wind turbine is still a relatively new research area, there is no detailed study on design optimization and coupled dynamics analysis. The optimal model must not only have favorable aerodynamic and hydrodynamic performance, but also satisfy the financial requirements. The aim of the present study is to conduct a detailed design optimization and numerical simulation of a mono-column tethered at the seabed mounted with a 5 MW turbine, based on the SWAY concept. We first introduce the numerical method used in the present study. We then present the design criteria employed and the final optimal SWAY model. Using a coupled dynamics numerical analysis, we investigate the dynamic performance of the optimal model. The detailed procedure to model a tether with swivel connection in Fatigue, Aerodynamics, Structures, and Turbulence (FAST) can be found in [32] and can be used in the present study. We also compare our optimization SWAY model with a reference model with a hinged connection at the fairlead. All these comparisons have demonstrated the SWAY model to be a good candidate for deepwater FOWT deployment.

2. Numerical Method

2.1. Aerodynamics Modeling

A wind turbine is a device that converts wind kinetic energy into useful output in the form of electrical power. The change of the pressure and the angular momentum when the wind passes across the rotor blades produces a lift force (normal to the inflow air) and a drag force (parallel to the inflow air), which generates the thrust and torque on the rotor and a pitch moment on the system.

In the present study, we use the AeroDyn subroutine package in FAST [7,12], to model and calculate the turbine aerodynamics through the classic blade-element/momentum (BEM) theory. The BEM method is the most commonly used tool to calculate the steady contribution of aerodynamic forces. We also include dynamic-stall behavior to consider the unsteady effects, such as the stall phenomenon based on previous models [33]. In FAST, the blades and tower flexibility are characterized by a linear model representation, based on the small deflection assumption within each member. These elastic characteristics are defined by inputting the distributed mass and stiffness factors for each member, and by prescribing their mode shapes as equivalent polynomials. In FAST, the two flap-wise and one edgewise mode of the blade and the two fore-aft and two side-to-side mode shapes of the tower are allowed, as illustrated in Figure 1. The nacelle and hub are modeled in FAST as rigid bodies. The tower is assumed to cantilever to the supported structure rigidly. Horizontal-axis wind turbines (HAWT) are used in the present study. We list the general properties of the 5MW wind turbine adopted in the present study in Table 1.

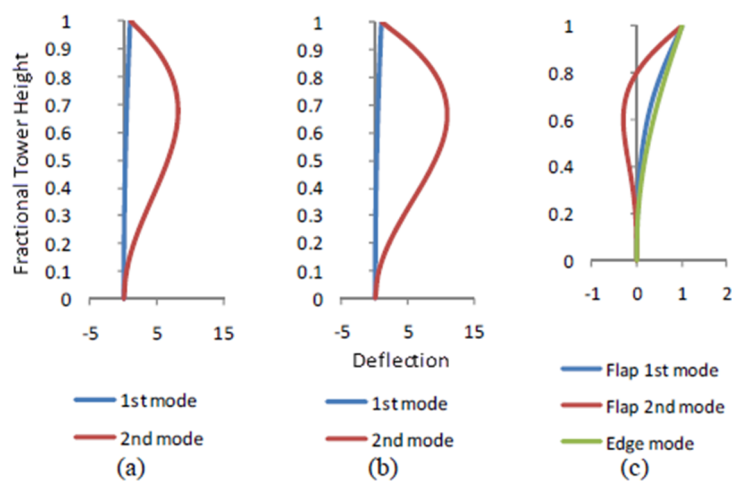


Figure 1. Normalized mode shapes: (a) tower fore-aft; (b) tower side-to-side; (c) blades flapwise and edgewise mode.

Table 1. General properties of the National Renewable Energy Laboratory (NREL) 5 MW baseline wind turbine.

Parameters	Value
Rating	5 MW
Rotor orientation, configuration	Upwind, three blades
Control	Variable speed, collective pitch
Drivetrain	High speed, multiple-stage gearbox
Rotor, hub diameter	126 m, 3 m
Hub height	90 m
Cut-in, rated, cut-out wind speed	3 m/s, 11.4 m/s, 25 m/s
Cut-in, rated rotor speed	6.9 m/s, 12.1 rpm
Rated tip speed	80 m/s
Overhang, shaft tilt, precone	5 m, 5°, 2.5°
Rotor mass	110,000 kg
Nacelle mass	240,000 kg
Tower mass	249,718 kg
Center of moment	(−0.2 m, 0.0 m, 70.4 m)
Rating	5 MW

The nacelle of the wind turbine is a structure housing the generator and drivetrain, mounted on the tower top through yaw bearing with a certain yaw mechanism of spring and damping. For the wind turbine used, the hub, at 90 m above the mean sea level (MSL), is located 5 m upwind of the

tower centerline when the system is undeflected. The vertical distance from the hub height to the tower top is 2.4 m, such that the elevation of the yaw bearing point above MSL is 87.6 m.

In the nacelle, the drivetrain consists of a gearbox, which is assumed to be typical multiple-stage with frictional losses, and the journal and thrust bearings, which support the shafts and minimize the movement of the drivetrain. With the torque generated by the lift force, the gearbox is used to step up the rotor output shaft to spin the electric generator. Then, the generator converts the mechanical work input of the wind turbine into useful electrical output. The slip, difference between the generator rotor frequency and rotating magnetic field determine the amount of power produced.

Since wind speed increases with height above ground, it is desirable to raise the wind turbine nacelle and rotor to take advantage of this effect. However, the height of the tower is determined by the rotor stiffness, which should be restricted such that there is no dynamic coupling between the rotor and the tower. The present study adopts the tower of the 5 MW baseline wind turbine for the Hywind-OC3 case [34]. The base of the tower coincides with the top of the platform at an elevation of 10 m above the MSL, while the top of the tower is coincident with the yaw bearing at an elevation of 87.6 m.

2.2. Hydrodynamics Modeling

We introduce a six-DOF rigid body with small rotational motions in Figure 2 for the support platform kinematics. Modes 1–3 represent translational surge, sway, heave displacement, and modes 4–5 represent angular motions about the x, y, and z axes (roll, pitch, and yaw). This inertial coordinate system of the platform is fixed to the mean location of the structure, with its $z = 0$ plane coinciding with the Mean Water Level (MWL). The wind and wave directions are in the positive x-direction throughout the static and dynamic analyses of the platform in the following paper.

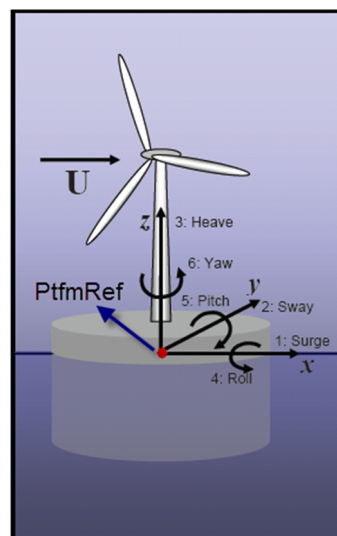


Figure 2. Six degrees of freedom motions of the oceanic floating offshore wind turbines (FOWT).

For wind turbines in the offshore environment, the loads acting on the platform mainly include hydrostatics $F_i^{hydrostatic}$, excitation forces from incident waves F_i^{exc} , and the restoring forces from tether lines F_i^{lines} . The total force $F_i^{platform}$ can thus be expressed as:

$$F_i^{platform} = -(M_{ij} + A_{ij})\ddot{q}_j + F_i^{exc} + F_i^{hydrostatic} + F_i^{lines} - \int_0^t K_{ij}(t - \tau)\dot{q}_j(\tau)d\tau. \quad (1)$$

Here, q is the body displacement and M_{ij} is the (i,j) component of the inertia mass matrix. K_{ij} is the retardation kernel and can be expressed as

$$K_{ij}(t) = \frac{2}{\pi} \int_0^\infty B_{ij}(\omega) \cos(\omega t) d\omega. \tag{2}$$

where A_{ij} and B_{ij} are the added mass and damping coefficient, respectively. In the present study, F_i^{exc} , A_{ij} and B_{ij} were obtained from [32] with an indoor program, HydroGen, which can generate the same hydrodynamic outputs as WAMIT [34]. Equation (1), which includes coupled resorting terms (e.g., shown in Tables 2 and 3), is a weakly nonlinear approach based on Cummins' equation [35]. The detailed expressions of the terms in Equation (1) will be further described in the following sections.

Table 2. Hydrostatic and gravitational restoring coefficients.

Hydrostatic Restoring Coefficients	Unit	Expression
$C_{33,H\&G}$	N/m	$\rho g A_0$
$C_{35,H\&G} = C_{53,H\&G}$	N	$-\rho g \iint_{A_0} x dA$
$C_{44,H\&G}$	Nm	$\rho g \iint_{A_0} y^2 dA + \rho g V_0 Z_{CB} - mg Z_{CG}$
$C_{55,H\&G}$	Nm	$\rho g \iint_{A_0} x^2 dA + \rho g V_0 Z_{CB} - mg Z_{CG}$

Table 3. Restoring coefficient of the single tether.

Tether Restoring Coefficients	Unit	Expression
$C_{11,tether} = C_{22,tether}$	N/m	T_0/L
$C_{33,tether}$	N/m	EA/L
$C_{44,tether} = C_{55,tether}$	Nm	$T_0 D^2/L$
$C_{15,tether} = C_{51,tether}$	N	$T_0 D/L$
$C_{24,tether} = C_{42,tether}$	N	$T_0 D/L$

2.2.1. Wave Excitation Force

The Froude-Krylov (F-K) and diffraction forces and moments are the compositions of the wave excitation load F_i^{exc} on the rigid body. The F-K force is due to the unsteady pressure field induced by the corresponding undisturbed waves with amplitude A , frequency ω and wavenumber k . The undisturbed F-K pressure for water depth h is written as Equation (3),

$$p_{FK} = -\rho \frac{\phi_I}{\partial t} = \rho g A \frac{\cos hk(z+h)}{\cos hkh} \sin(\omega t - kx), \tag{3}$$

where ρ is the water density and ϕ_I is the velocity potential for the incident wave. The undisturbed pressure field would exist only if the body is "transparent" to the wave motion, which is physically impossible. Therefore, there must be a force, wave-scattering force, accounting for the additional pressure distribution due to the body's presence. The summation of the incident wave potential ϕ_I and the scattered wave potential ϕ_S is defined as the diffraction potential ϕ_D . Then, the total wave excitation force can be found in the Equation (4), with the first and second term being the F-K force and the scattering wave force, respectively.

$$F_i^{exc} = - \int_{SB} \rho \frac{\phi_D}{\partial t} n_i ds = - \int_{SB} \rho \frac{\phi_I}{\partial t} n_i ds - \int_{SB} \rho \frac{\phi_S}{\partial t} n_i ds, \tag{4}$$

where,

$$\phi_D = \phi_I + \phi_S; \quad \frac{\phi_S}{\partial n} = -\frac{\phi_I}{\partial n}. \tag{5}$$

2.2.2. Hydrostatics Force

Hydrostatic loads include buoyancy force and hydrostatic restoring forces, which are written as:

$$F_i^{hydrostatic} = \rho g V_0 \delta_{i3} - C_{ij,H\&G} q_j. \quad (6)$$

Here, $\rho g V_0 \delta_{i3}$ is the buoyancy force, and $C_{ij,H\&G}$ is the (i,j) component of the linear hydrostatic-restoring matrix. In the present study, the hydrostatic restoring coefficients are expressed by a linear hydrostatic and gravitational restoring matrix, whose nonzero coefficients are given in Table 2.

2.2.3. Tether Forces

For the present model, the tether system includes only one single taut tether. The structure achieves stability with an additional buoyancy, which increases the pretension of the taut tether. The displacement caused by the external loading on the floater is resisted by the restoring force produced by the tethers. As shown in Equation (7), we apply a quasi-static model to calculate the total load given by tether on the support platform F_i^{lines} . $C_{ij,tether}$ is the linearized restoring matrix and $F_i^{lines,0}$ represents the pretension at the fairleads.

$$F_i^{lines} = F_i^{lines,0} - C_{ij,tether} q_j. \quad (7)$$

By applying the small displacement approximation, the draft and the tether tension can be considered as constant, and the stiffness $C_{ij,tether}$ provided by the single tether is shown in Table 3, where T_0 is the pretension provided by the excess buoyancy, L is the unstretched length of the single tether, D is the draft of the submerged body, and EA is the extensional stiffness. As shown in Table 3, the coupling between the surge/heave is nonlinear, and determined by the length of the tethers. These coupling effects also provide additional stability to the system through the restoring force produced by the tethers.

2.3. Coupled Aero-Hydro-Dynamics Algorithm

The fully dynamic coupling between the supported platform's motion and the wind turbine is critical in establishing the equation of motion for the whole system. Equation (8) gives the general form of the nonlinear time-domain equation of motion adopted in FAST for the coupled wind turbine and support platform system used in the present study.

$$M_{ij}(q, u, t) \ddot{q}_j = f_i(q, \dot{q}, u, t). \quad (8)$$

Here, M_{ij} is the (i,j) component of the inertia mass matrix, q is the system degree of freedom (DOFs), u is the control input, t is time, and f_i is the forcing function of the system. Figure 3 shows the numerical scheme for the coupled dynamics analysis in the present study. This flowchart combines the steady-state frequency-domain solutions, the wave simulations, time-domain hydrodynamic-loading calculations, and the nonlinear structural-dynamic-coupling module. HydroGen, an indoor program, can generate the same hydrodynamic outputs as WAMIT [36], and acts as the preprocessor for the coupled dynamics analysis of the interaction between surface waves and the SWAY model.

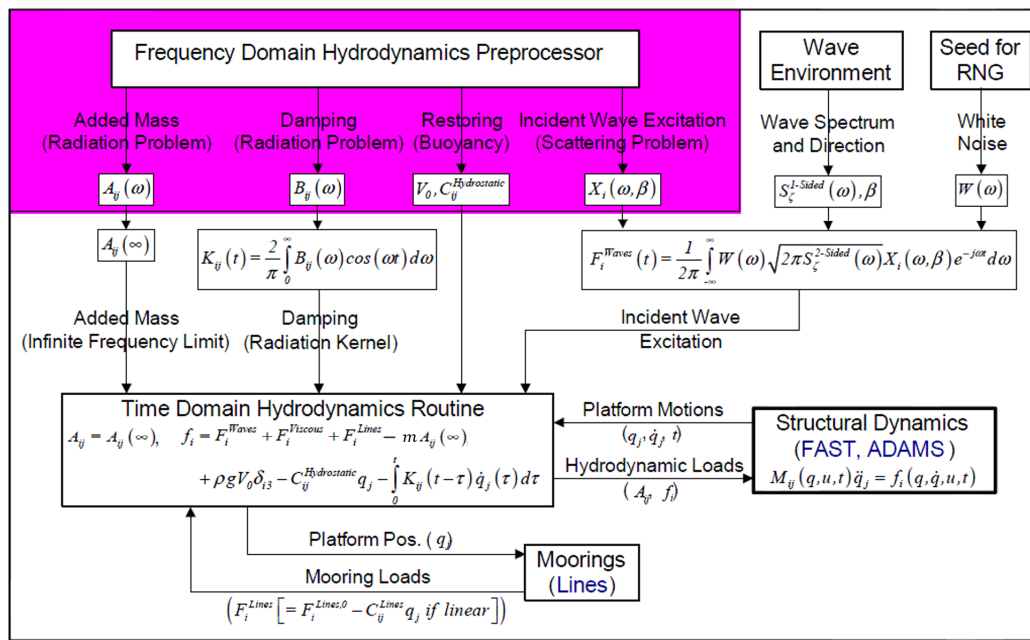


Figure 3. Flowchart of calculations for the total external loads on the support platform.

3. Optimization Criteria and Results

The following section first presents the optimization criteria, including the static, dynamics, and cost criteria. Based on these criteria, we then obtain and present the optimized model. The wind conditions and the corresponding thrust and moment used for optimization is based on the rated wind conditions for the NREL 5 MW wind turbine [16]. These parameters, shown in Table 4, are treated as constant throughout the optimization.

Table 4. Design constants for the optimization process.

Inputs	
Wind turbine	NREL 5 MW
Rated wind speed	11.4 m/s
Maximum thrust	800 kN
Turbine moment	72,000 kN·m
Freeboard	10 m

3.1. Static Criteria

The first criterion is to demonstrate the acceptable static performance in its installed state, which is defined as the static design criteria. Equation (9) demonstrates the fully coupled governing time-harmonic equation of motion, where all coefficient matrices are about the three system components: wind turbine (consisting of the rotor, nacelle, tower), platform, and tether system.

$$F^{exc}(\omega)e^{i\omega t} = [A_{add}(\omega) + M]\ddot{q} + [B_{rad}(\omega) + B_{external}]\dot{q} + [C_{H\&G} + C_{external}]q. \quad (9)$$

Here, the hydrodynamic coefficients include the added mass matrix, $A_{add}(\omega)$, the platform radiation damping matrix, $B_{rad}(\omega)$, and the wave excitation force, $F^{exc}(\omega)$, which are all functions of frequency. M is the total mass matrix of the system, including the wind turbine and the support platform. $B_{external}$ is the external damping from the wind turbine. $C_{H\&G}$ is the linear hydrostatic and gravitational matrix of the platform. $C_{external}$ is the external stiffness matrix provided by the wind turbine and tether. q represents the response motion of the 6DOFs modes for the structure.

Velocities and accelerations are zero in static, and only static forces and moments exist. Under these conditions, Equation (9) reduces to

$$F_{static} = [C_{H\&G} + C_{tether}]q(\omega), \quad (10)$$

3.1.1. Pitch Restoring Coefficient

In the present study, a 10-degree pitch angle is defined as the static threshold. Beyond the angle (i.e., $q_{5, Lim} = 10^\circ$) in which the wind turbine will lose the substantial efficiency is used to determine the minimum value of the pitch restoration. We choose the maximum turbine moment as $M_5 = 7200 \text{ kN}\cdot\text{m}$, which corresponds to the static thrust $F_{thrust} = 800 \text{ kN}$ at a wind speed of 11.4 m/s acting on the turbine hub, at $z_{hub} = 90 \text{ m}$. Equation (11) expresses limitation of C_{55} as

$$C_{55, Lim} = \frac{M_5}{q} = \frac{F_{thrust}z_{hub}}{q_{5, Lim}} = \frac{800 \times 90 [kN\cdot m]}{10^\circ \pi / 180^\circ} = 4.126 \times 10^8 [N\cdot m], \quad (11)$$

The pitch restoration coefficient C_{55} for the present model can then be obtained from Equation (12). Here, R is the cylinder radius, D is the platform draft, T_0 is the tether pretension, ρ is the seawater density, L is the total unstretched length of the tether, Z_{CB} and Z_{CG} are the center of bounce and center of gravity, respectively, and V_0 is the displacement of the offshore wind turbine.

$$C_{55} = C_{55, H\&G} + C_{55, tether} > C_{55, Lim}, \quad (12)$$

3.1.2. Surge Restoring Coefficient

The tether tension for this system should not only fulfill the restoring requirements for the restrained pitch angle, but also provide sufficient restoring force to limit the surge displacement adequately. The criteria for surge displacement is that the angle θ formed by the tether and the vertical axis should be limited under five degrees, to prevent the system from experiencing a highly nonlinear restoration and displacement. Similar to Equation (12), surge restoration from the tether is related to pretension and tether length with the limit, as shown in Equation (13).

$$C_{11} > C_{11, lim} = \frac{F_{thrust}}{q_{1, Lim}}, \quad (13)$$

where $F_{thrust} = 800 \text{ kN}$ and $q_{1, Lim} = 5^\circ \pi / 180^\circ \cdot L$.

3.2. Dynamics Criteria

3.2.1. Natural Frequency

As the optimization process to the dynamic phase, the most crucial step is to find out the natural frequencies of the coupled system in six modes of motion, which should not coincide with the peak frequency of the dynamic loading. We express the natural frequency for the i^{th} motion modes as

$$\omega_i = \sqrt{\frac{C_{ii}}{M_{ii} + A_{ii}(\omega)}}, \quad (14)$$

where the $A_{ii}(\omega)$ indicates the added mass, M_{ii} is the total mass of the system, and C_{ii} is the total restoring stiffness, consisting of contributions from the wind turbine, the platform, and the tether. The natural frequencies of the motions should be designed to avoid resonance by setting the natural frequencies beyond the range of dominant wave frequencies (0.2–2.5 rad/s). Resonance effects due to the time-varying loads from the wind turbine can also occur. To avoid this, the natural frequencies of the coupled system should not coincide with rotor frequency (1P) and the tower flexibility frequency or the blade passing frequency range (3P). For a NREL 5 MW baseline wind turbine at rated wind

speed, the rotor speed is 12.1 rpm, such that the corresponding rotor frequency 1P equals 1.256 rad/s, and the blade passing frequency 3P is 3.801 rad/s. To facilitate the control and optimization of natural frequency, we conducted a parameter study to determine the effect of design parameters on the system dynamic responses. We found that the main parameters that determine the natural frequency of the systems, are the draft D , bottom diameter R , and tether stiffness, as shown in Figure 4. Based on similar study for TLP type platform [37], we present the impact of the main parameters on C_{ii} , M_{ii} , and A_{ii} on the natural frequency ω_i in Table 5.

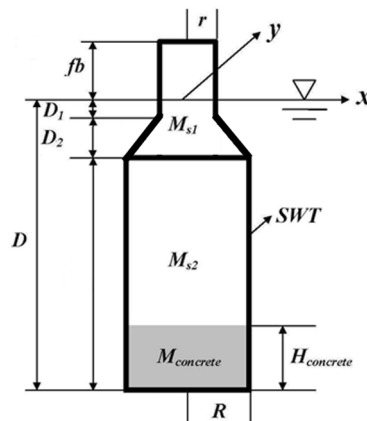


Figure 4. Sketch of support platform for the SWAY model.

Table 5. Parameters’ influences on the natural frequencies of SWAY model (↑: increase; ↓: decrease; -: negligible effect).

Parameters	C_{ii}				M_{ii}				A_{ii}				ω_i				
	i	1	3	5	6	1	3	5	6	1	3	5	6	1	3	5	6
↑ R	↑	-	-	-	↑	↑	↑	↑	↑	↑	↑	-	↑	↓	↓	↑	
↑ D	↑	↑	↑	-	↑	↑	↑	↑	↑	↑	↑	-	↑	↓	↓	↑	
↑Tether extensional stiffness	-	↑	-	-	-	-	-	-	-	-	-	-	-	↑	-	-	

3.2.2. Dynamic Tether Tension

For the present model, which contains only one taut tether, it is particularly important to consider the tether tension’s variation during operation, since the tether’s failure will directly lead to the whole system capsizing. The dynamic tether tension should not exceed the breaking load of the tether within a safety factor, but should also prevent failure via a buckling load. The expressions for the tether tension constraint dynamics are given in Equations (15) and (16). Here, $T_{tether,fairlead}$ and $T_{tether,anchor}$ are the dynamic tether tensions at the fairlead and anchor point, respectively; σ represents the standard deviation of the tether tension at the fairlead and anchor; and $F.S.$ is the factor of safety, which is usually chosen as 1.5–2.0, based on the previous study [4].

$$(T_{tether,fairlead} + \sigma_{tether,fairlead})F.S \leq T_{max}, \tag{15}$$

$$(T_{tether,anchor} - \sigma_{tether,anchor})F.S \geq 0, \tag{16}$$

3.3. Cost Criteria

To ensure that the floating configurations are competitive with bottom-fixed configurations at intermediate water depths, the steel mass must be less than 1000 metric tons. Based on the quotes from several manufactures and previous studies [4], we estimate the cost of steel, concrete, and tether.

We set the cost of steel between \$600 and \$800 per metric ton. The concrete ballast that is located at the bottom of the cylinder can also make a significant contribution to the cost, and the price is in a range from \$50 to \$150 per metric ton. The tether system can account for a large part of the cost of the whole system. The anchor cost per kilonewton tether tension is estimated to be between \$15 and \$25. In the present study, the costs for steel, concrete, and tether tension are used to calculate and minimize the entire building costs of the FOWT, while maintaining the static and dynamics criteria.

3.4. Optimization Procedure

3.4.1. Step 1: Cost and Stability

The mass density of concrete is nearly 2.56 times higher than water density. It is thereby much more efficient to use concrete ballast to satisfy the spar-buoy type platform’s stability requirements: the center of gravity (CG) is far below the center of buoyancy (CB), and the total weight of the platform is equal to the buoyancy force. Besides, it is important to make the hydrostatic coefficients positive, to ensure its stability in case of the single tether system. Therefore, with the top mass and platform draft being known, the main work of the first step is to determine the acceptable platform diameter and the height of the concrete ballast for multiple cases with different platform steel wall thickness (SWT). Here, we show results with SWT = 0.015 m, 0.0253 m, 0.045 m as an example.

The platform diameter is an important parameter determining the system buoyancy, steel mass, variables that influence the CG, pretension, and cost directly. In Figure 5, we show the results of platform diameters R in the range from 11 m to 13 m. Figure 5 shows that the minimum concrete height $H_{concrete}$ can be found to keep both hydrostatic and gravitational restoring coefficients positive. For all cases, this restoring coefficient will increase with a larger platform diameter and a higher concrete ballast, which means better static stability at the same time. In Figure 5, the lower and upper limits of the total cost are also shown for different diameters. By comparing the total cost between these three cases, it is evident that the system costs much more with SWT = 0.045 m. On the other hand, for the same SWT, the total cost increases with a larger diameter and decreases with the increase of concrete ballast height. We can thus conclude that steel mass is the main cost driver in the support platform design.

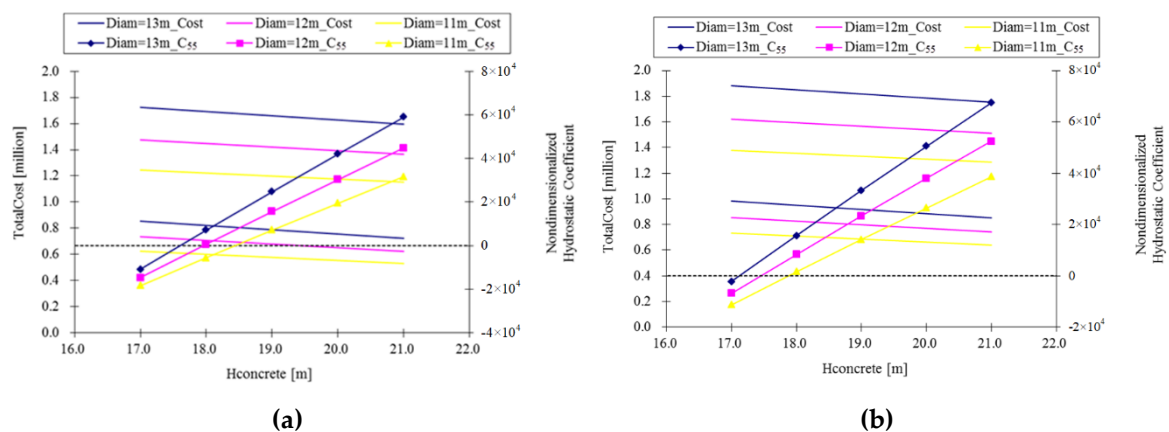
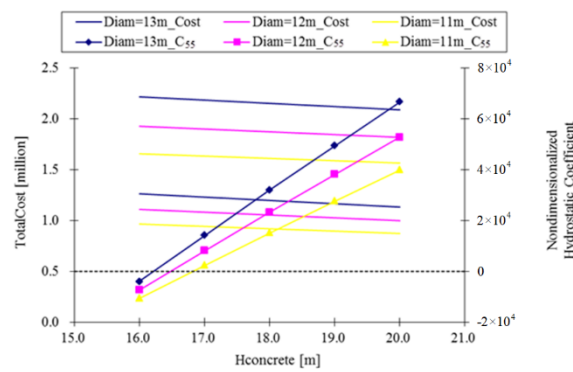


Figure 5. Cont.



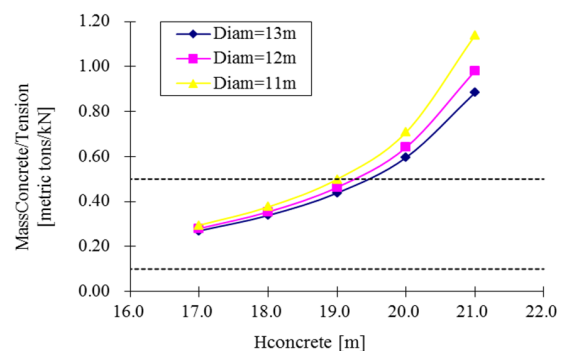
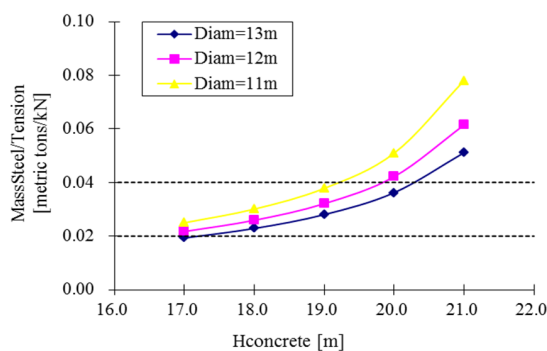
(c)

Figure 5. Hydrostatic stiffness and total cost for three cases: (a) platform steel wall thickness (SWT) = 0.015 m; (b) SWT = 0.0253 m; (c) SWT = 0.045 m. The solid line without a marker represents the upper and lower limits for the platform cost of the corresponding $H_{concrete}$. The black dash line represents when hydrostatic coefficient equals 0.

Based on the cost and tension discussed in Section 3, the design can be close to cost-optimized when it fulfills the design limits that steel mass/tether tension is in the range of approximately 0.02 to 0.04, while concrete mass/tether tension is in the range of 0.1 to 0.25. Figure 6 shows that the case with SWT = 0.045 m has been significant out of the optimized economic range. Figure 6 also demonstrates that the mass property ratio decreases with platform diameter, while it increases with the concrete ballast. From these results, we obtain a range of concrete ballast heights, by considering both basic stability requirements and cost drivers. We summarized the results of step 1 in Table 6. The following steps 2 and 3 are also necessary to see whether these cost-optimized designs also satisfy other considerations. When ensuring the design’s safety is necessary, the above iterative process needs to be repeated, even to increase these optimized mass property ratios.

Table 6. Design result for concrete ballast height from step 1.

Diameter (m)	Case 1: SWT = 0.015 m	Case 2: SWT = 0.0253 m
13	17.7–19.4	17.2–17.4
12	18.0–19.2	–
11	18.5–19.0	–



(a)

Figure 6. Cont.

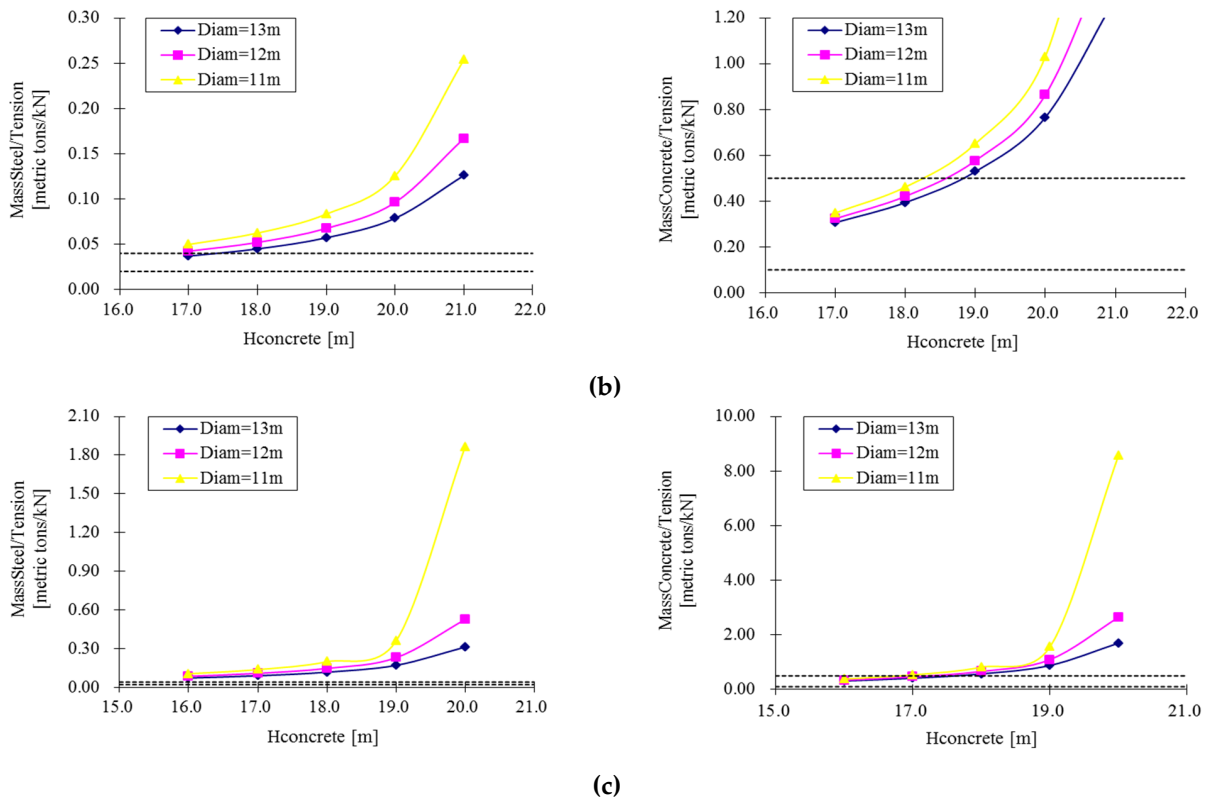


Figure 6. Optimized mass property ratio for three cases with SWT = (a) 0.015 m; (b) 0.0253 m and (c) 0.045 m. The region between the black dash lines represents the optimized cost regions.

3.4.2. Step 2: Restoring Forces

As shown in Equation (10), the minimum pitch restoring coefficient, $C_{55,Lim}$, equals 4.126×10^8 Nm, to ensure that the pitch angle is less than 10 degrees. As for the surge restoring coefficients, its limit value is related to water depth. Here, we show examples with 200m water depth. The unstretched length of the taut tether is 128 m in such a case. Based on Equation (13), the minimum surge restoring coefficients, $C_{11,Lim}$, are 71710 N/m. Figure 7 presents the surge and pitch restoring coefficients, from which the range of concrete ballast height can be further narrowed. Figure 7 shows that both surge and pitch restoring coefficients increase with platform diameter. However, when the concrete ballast height increases, the pitch restoring coefficients increase, while the surge restoring coefficients decrease. We further narrow the concrete heights from step 1 results, as well as the value corresponding to the intersection of surge and pitch restoring coefficients in Figure 7. We summarize these results in Table 7.

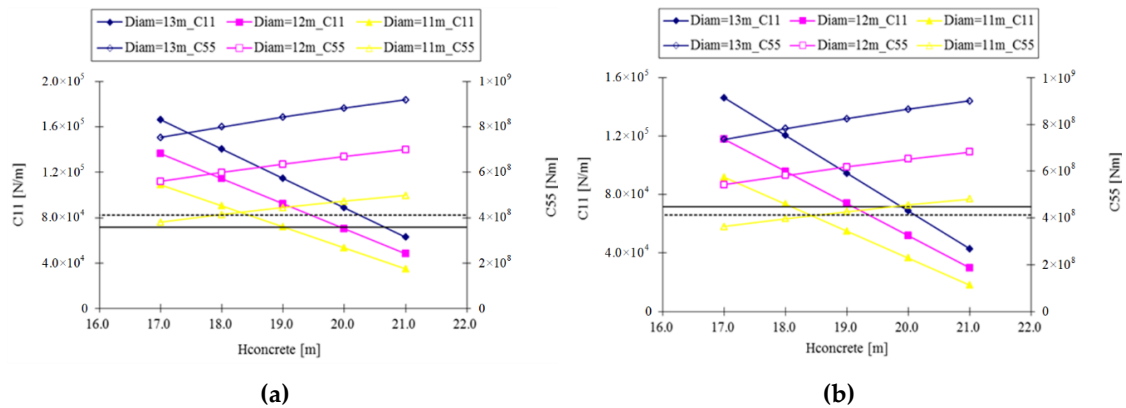
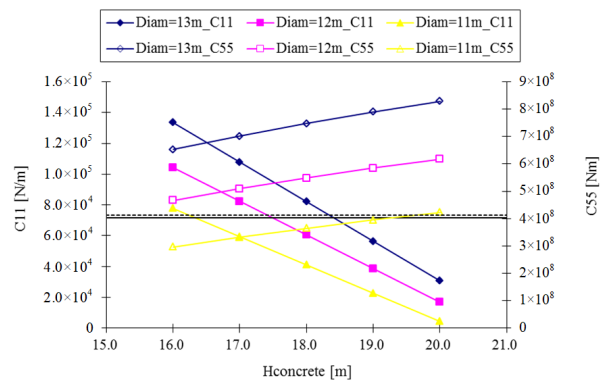


Figure 7. Cont.



(c)

Figure 7. Surge and pitch restoring stiffness for three cases with SWT = (a) 0.015 m, (b) 0.0253 m, (c) 0.045 m. The solid black line is the lower limit for C₁₁, while the black dash line represents the lower limit for C₅₅.

Table 7. Properties of the optimized design after Step 2.

Properties	Case1		Case 2	
	SWT = 0.015 m		SWT = 0.0253 m	
Diameter (m)	13	12	11	13
Hconcrete (m)	17.9	18.2	18.7	17.4
Hydrostatic coefficient	5321.1	3572.8	3312.4	4944.5
Total cost_lower (million)	0.82441	0.70121	0.5841	0.97024
Total cost_upper (million)	1.69536	1.4423	1.20546	1.86954
Pretension (kN)	18,324.5	14,085.7	9922.1	17,403.3
Surge restoring coefficient (kN/m)	143.16	110.04	77.52	135.96
Pitch restoring coefficient (kNm)	795,629.3	606,385.2	435,140.4	754,534.1
Surge natural frequency (rad/s)	0.09459	0.08904	0.08052	0.09192
Pitch natural frequency (rad/s)	0.13242	0.12397	0.11299	0.12908
Total mass (metric tons)	7065.38	6222.45	5472.75	7159.32
Total displacement (metric tons)	8933.99	7658.82	6484.54	8933.99

3.4.3. Step 3: Natural Frequencies

Based on Equation (14), we calculate the natural frequencies in surge and pitch modes. Figure 8 shows that the natural frequencies in surge and pitch are all below 0.14 rad/s, which is out of the energy-concentrated region in wave spectrums (e.g., Figure 12).

Based on the API 5L steel pipe dimension and weight information, as well as the steel hardness of various types of tubes in the manufactory, we choose the steel tether with 603 mm diameter, 44 mm thickness, and the steel hardness type is API 5L X65, whose yield strength is 60200 psi (1 pound in square inch). In this case, the line mass per unit length is 606.57 kg/m, the EA stiffness is 1.62×10^{10} Nm, and the maximum allowable tension is 3.48×10^7 N, much larger than the pretension. With the tether properties defined, we find the heave natural frequency among the platform geometry from step 2. The natural frequencies in heave motion shown in Table 8 are much larger than 2.5 rad/s, the upper boundary of the energy concentrated regions in the wave spectrum.

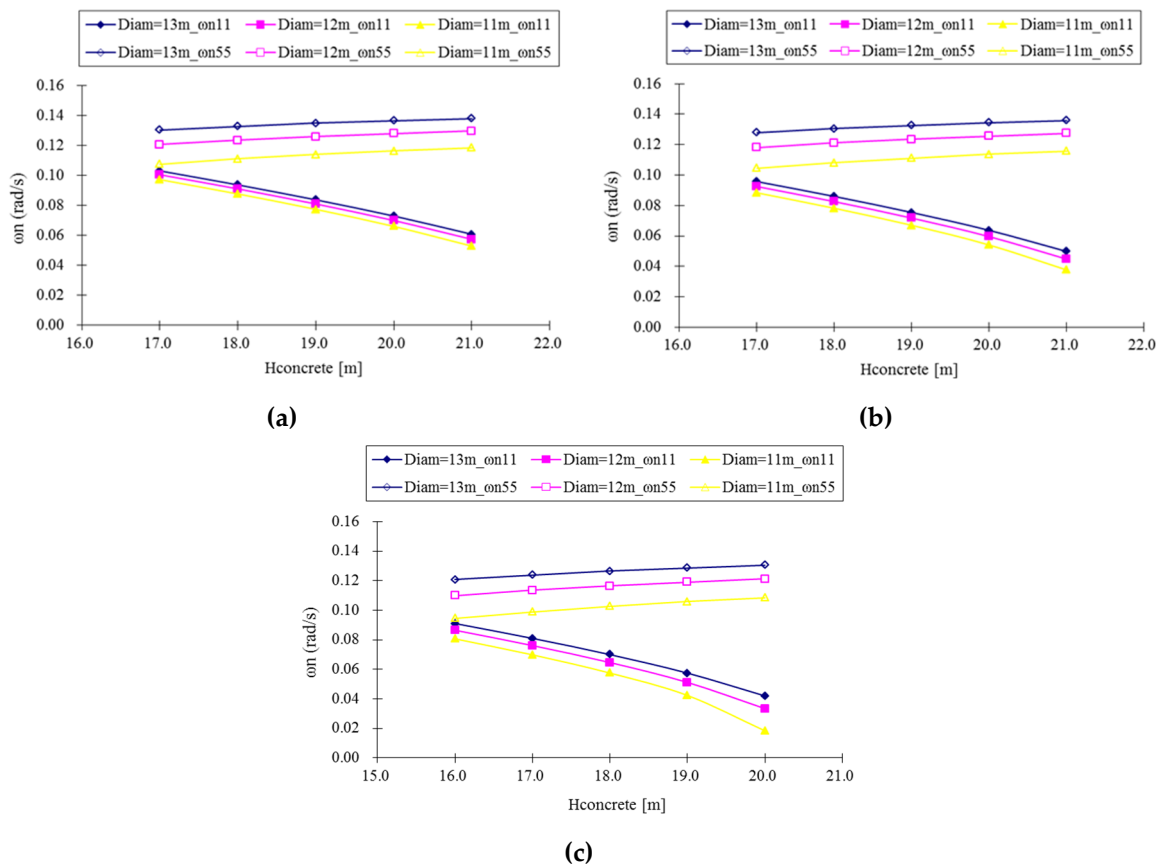


Figure 8. Surge and pitch natural frequencies for three cases with SWT = (a) 0.015 m, (b) 0.0253 m, (c) 0.045 m.

Table 8. Heave natural frequencies of optimized designs.

Steel Wall Thickness (m)	Diameter (m)	$H_{concrete}$ (m)	ω_{n33} (rad/sec)
Case 1 = 0.015 m	13	17.7	4.19561
		19.4	4.03792
	12	18.0	4.46077
		19.2	4.34475
		18.5	4.74421
Case 2 = 0.0253 m	13	19.0	4.69420
		17.2	4.16852
	17.4	4.14944	

3.5. Optimized Model

In the present study, we find a model that satisfies all the design criteria discussed above through an iterative optimization process. The optimization mainly focuses on the controllable parameters during the design process: the diameter of the platform (optimization range: 11 m–12 m), the height of the platform concrete base $H_{concrete}$ (optimization range: 17 m–21 m), and the steel wall thickness (optimization range: 0.15 m–0.45 m). The range for the optimization is based on similar previous studies (e.g., [4,16,19]). Using the trial and error algorithm, we obtain and select from more than 100 potential models, to meet the static and dynamic criteria and minimize the building costs. As shown in Table 9, we demonstrate the optimized model, which satisfies all the static, dynamic, and economic requirements.

Table 9. Optimized SWAY model parameters (we define $D, D_1, D_2, r, R, H_{concrete}$ in Figure 4).

Specifications	Unit	Optimized Model
D	m	72
D_1	m	4
D_2	m	8
r	m	6.5
R	m	13
$H_{concrete}$	m	18
Platform steel wall thickness (SWT)	m	0.015
Total cost	million dollars	0.82–1.69
Steel mass	metric tons	411.376
System mass	metric tons	7099.20
Center of gravity (System)	m	−50.1373
Total displacement	metric tons	8934
Center of buoyancy	m	−39.0355
Platform roll/pitch inertia about mean water level	kg·m ²	2.5134×10^{10}
Platform yaw inertia about the centerline	kg·m ²	1.4306×10^8
Pretension	kN	17992.8
Surge restoring coefficient	kN/m	140.57
Pitch restoring coefficient	kN·m	800,118.7
Max. allowable tether tension	kN	3.48×10^4
Line cross-area	m ²	0.0773
EA stiffness unit length	Nm	1.62×10^{10}
Line mass density	kg/m	606.57
Surge/sway natural frequency	rad/s	0.098
Heave natural frequency	rad/s	4.166
Pitch/roll natural frequency	rad/s	0.112
Yaw natural frequency	rad/s	0.713

4. Coupled Dynamics Analysis

The next step is to conduct the couple dynamics analysis to investigate the dynamic performance of the present model. The swivel connection design between the turbine support platform and the single tether is the most distinguishing property of the SWAY concept wind turbine. In the swivel connection offshore wind turbine shown in Figure 9a, the floating wind turbine is hinged to the seabed by a tensioned tether. This tether then connects to the turbine tower with a passive yaw swivel. Such swivel connection allows the offshore wind turbine tower to yaw together with the turbine, according to the wind directions. Such yaw mechanism is close to the weathervaning mechanism, which is similar to the turret mooring system for the floating production storage and offloading vessel (FPSO). When there are no wind conditions, the SWAY offshore wind turbine tower can still be rotated by running the generator to produce the rotor blades' pitching. To demonstrate the relative advantage of this design, a reference hinged model, in which the tether and platform are hinged at the connection, is also modeled and simulated, as shown in Figure 9b. We demonstrate the comparison of the swivel and hinged connection in Figure 9a,b. Both swivel and hinged connections allow the tower system to rotate freely in the yaw mode. However, the swivel connection differs from the hinged connection for its additional restriction on the rotational motions. Thus, the swivel connection increases the stability of the offshore wind turbine and reduces the wind turbine structure's damage rate. We will further demonstrate these features of the offshore wind turbine with a swivel connection in the present section. To be consistent with the SWAY concept, we also modified the 5MW wind turbine used in present study to downwind-orientation based on method in [32].

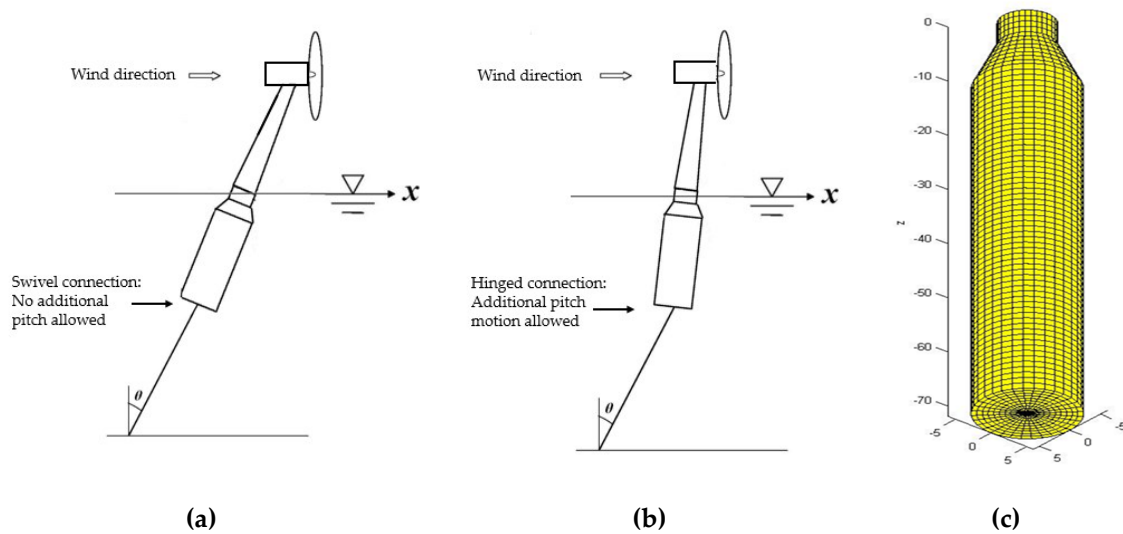


Figure 9. (a) Swivel connection model; (b) Hinged connection model; (c) numerical panel mesh for the support platform of FOWT.

We generate both models using HydroGen and FAST, and conduct a fully coupled dynamic analysis in the time domain. Figure 9c shows the numerical model of the platform hull. We model the platform with 656 quadratic panels within a quarter of the body. This section presents the simulation results of both the SWAY swivel and hinged models under the operational load cases listed in Table 10. We use the Jonswap spectrum to generate the irregular incident wave in the x-direction. The peak shape parameter γ for all the cases is 1.75. The time step of the simulation is selected as $\Delta t \approx T_p/100$. The total length of the simulation is $T_0 = 1$ h. The total amount of sample needed to assess the quantities is therefore $T_0/\Delta t$. The time series analysis window is from 500s to the end of the simulation after the transient and drift effects are damped out. The wave elevations for each case are generated independently six times. The total six sets of simulation results are then summarized to obtain the extreme values and standard deviations.

Table 10. Environmental conditions for coupled dynamics analysis.

Case Number	Wind Speed (m/s)	H_s (m)	T_p (s)
1	9	6	10
2	11.4	6	10
3	13	6	10
4	15	6	10
5	18	6	10
6	25	6	10
7	11.4	2.44	8.1
8	11.4	3.66	9.7
9	11.4	8	12.5
10	11.4	10	14

For all the numerical cases in Table 10, we find that the tether tension is mainly correlated to the platform's pitch motion and below the tension maximum. Additionally, the main loads are only applied in the x-direction for the numerical model. As a result, we select the surge and pitch displacements as the main parameters for analysis and comparison of the dynamic performance of the FOWT. To evaluate wind turbine performance, we also analyze and compare the inline nacelle velocity and acceleration.

4.1. Motion Comparison between Sway Model and the Reference Hinged Model

We first show the dynamic performance of the SWAY swivel model and the reference hinged model, under the second environment loading case defined in Table 10. Both wind and wave loads are applied in the x-direction only. We show the time-domain results of the platform motions in Figure 10. Figure 11 plots the spectra after the system is steady, such that the initial transient effect has been damped out. The wave elevation time series and spectrum of case 2 are present in Figure 12. As shown in the time series and spectra, the SWAY swivel model is mainly oscillating at its natural frequencies in 6DOFs. Compared to the reference hinged model, the resonant responses in the SWAY swivel in surge mode due to dynamic interaction between the hull and the turbine, as well as the wave frequency responses, are smaller.

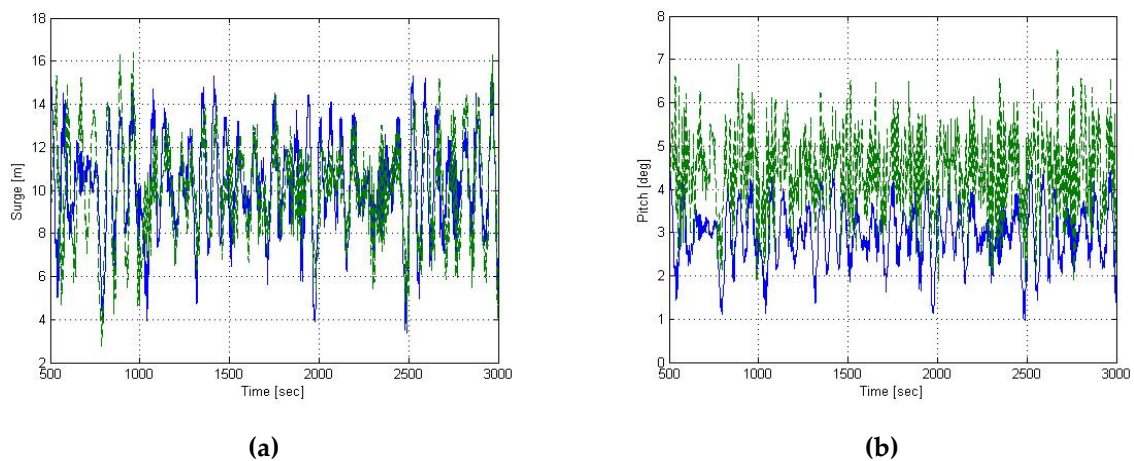


Figure 10. Platform responses time series of SWAY swivel and reference hinged model. (Solid blue: swivel model; Dash green: reference hinged model): (a) Surge. (b) Pitch.

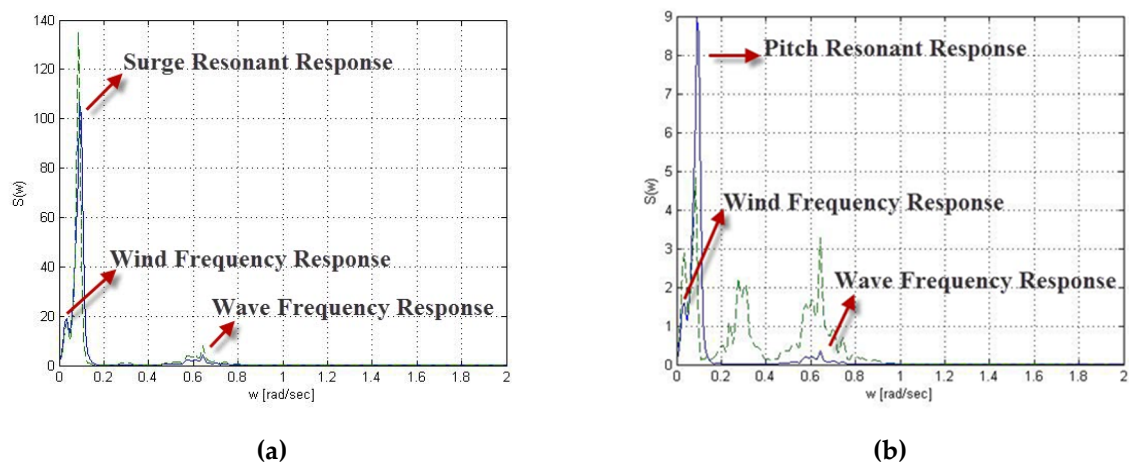


Figure 11. Platform response spectra of SWAY swivel and reference hinged model Case 2. (Solid blue: swivel model; Dash green: hinged model): (a) Surge. (b) Pitch.

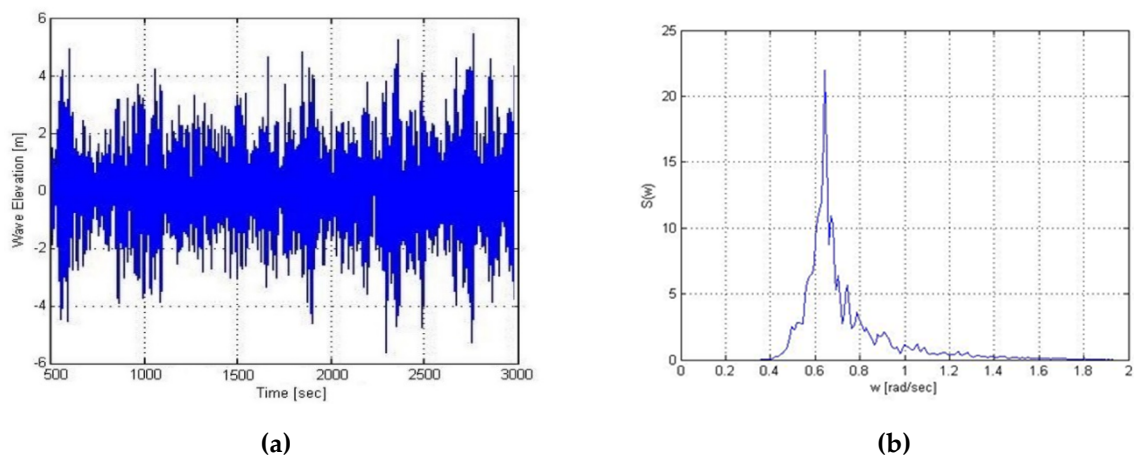


Figure 12. Environmental conditions for case 2: (a) Time series of wave elevation. (b) Wave spectrum.

We show the velocity and acceleration of the nacelle in Figure 13. These results are essential parameters to measure the performance of the wind turbines. As shown in Figure 13, the nacelle of the tower experiences smaller fore-aft velocity and acceleration in the SWAY model. We find that the fore-aft resonant response of the nacelle is mainly located in the range of wave frequencies shown in Figure 13. These results indicate that the SWAY swivel model has better dynamics and stability performance than the reference hinged model.

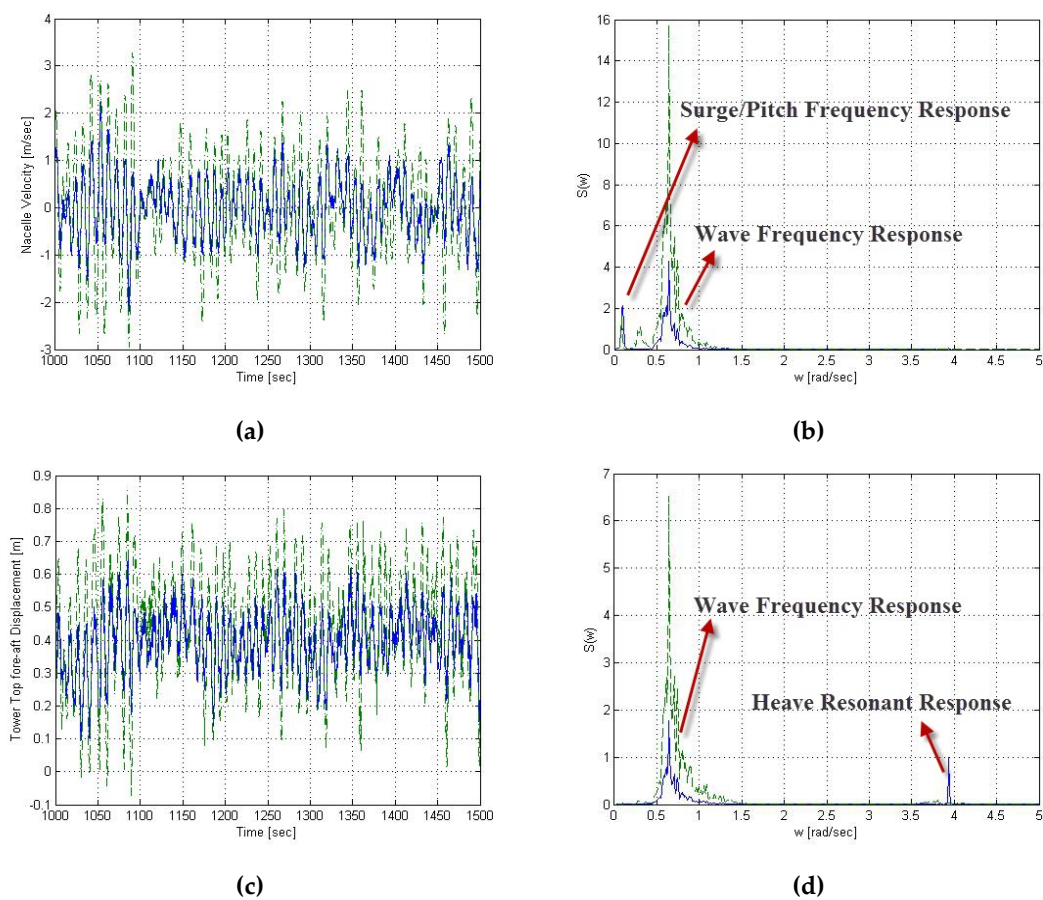


Figure 13. Tower top displacements of SWAY swivel model and reference model. (Solid blue: SWAY model; Dash green: reference hinged model): (a) Nacelle velocity time series. (b) Nacelle velocity spectrum. (c) Nacelle acceleration time series. (d) Nacelle acceleration spectrum.

4.2. Effect of Wind Speed

Figure 14a,b present the surge and pitch displacements for both the SWAY swivel model and the reference hinged model under a range of wind speeds. We find that the mean displacement for both the surge and pitch motions are highly dependent on the thrust force. From the comparison, we demonstrate that the surge displacements for both models are very similar, but the mean and standard deviations in the pitch motion of the SWAY swivel model are much smaller than the hinged model. This result again proved the ability of the SWAY swivel model to control the pitch motion. As shown in Figure 14c,d, we find that the standard deviations of the nacelle velocity and accelerations are close to constant for the range of operating wind speeds, except for a small increase of the nacelle velocity in the SWAY swivel model with $U_{mean} = 13$ m/s, where the oscillation of the whole system is quite large. From the comparison, the SWAY swivel model shows an advantage in performance compared to the reference hinged model, as the standard deviations of nacelle velocity and acceleration are much smaller.

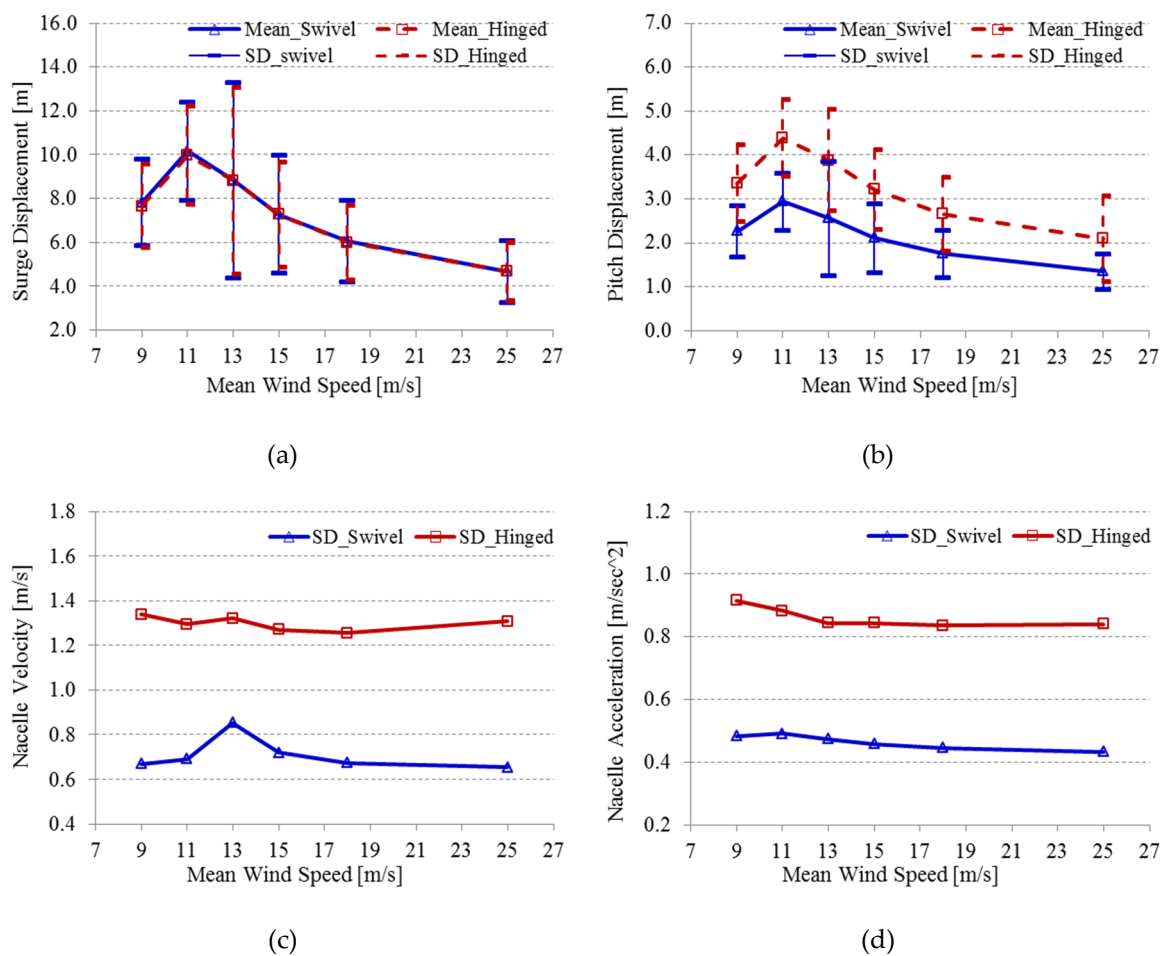


Figure 14. Wind effect on surge/pitch motions and turbine performance: (a) Surge motion. (b) Pitch motion. (c) Nacelle Velocity. (d) Nacelle Acceleration. SD: standard deviation.

4.3. Effect of Sea States

Figure 15a,b present the platform’s surge and pitch displacements for different significant wave heights. From the comparison, we demonstrate that the mean displacement values are constant for different significant wave heights. However, we note that the standard deviation of the surge and pitch displacements depend on the significant wave heights. The changing sea state had a smaller effect on the SWAY swivel model than the reference hinged model. We also observe smaller standard deviations

in the SWAY swivel model than the hinged model in Figure 15. These results indicate the superior performance of the SWAY swivel model.

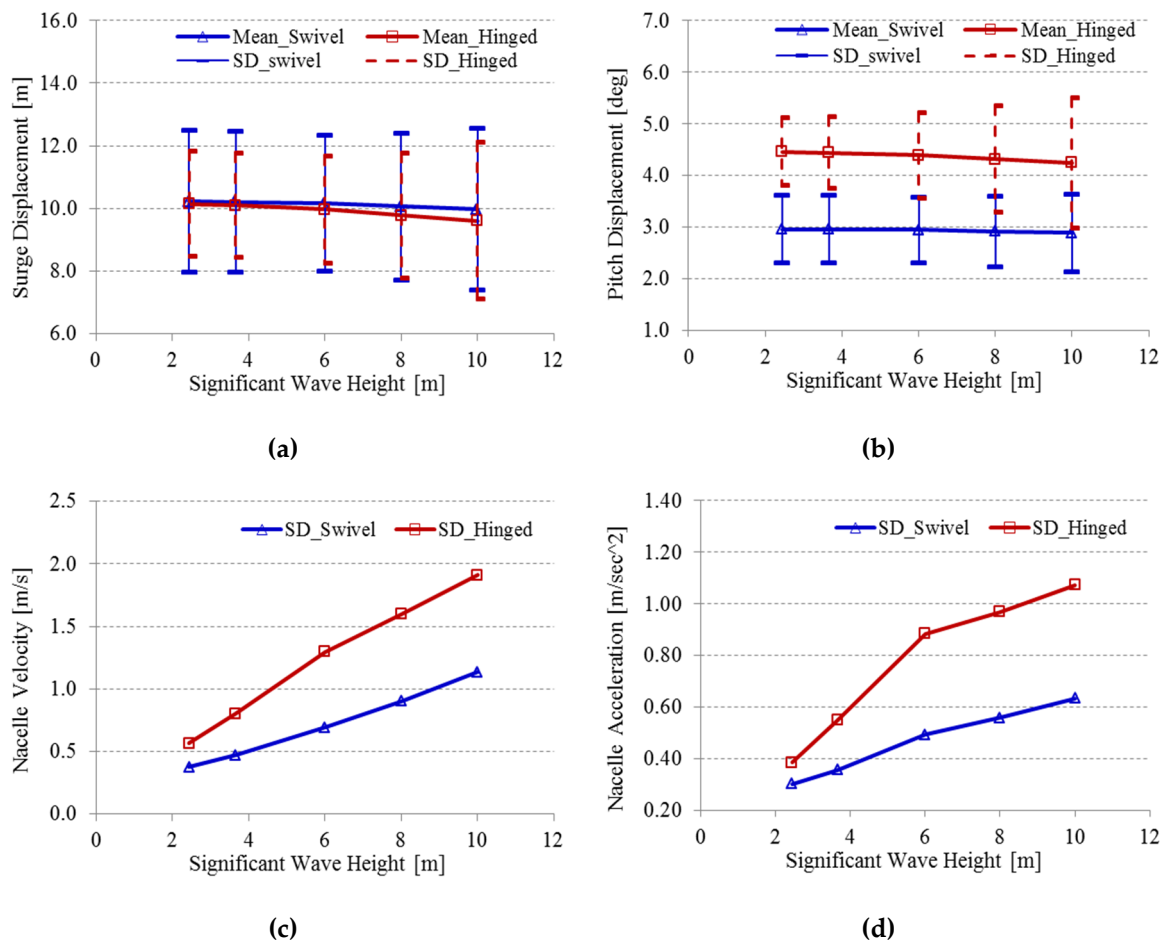


Figure 15. Wave effect on surge/pitch motions and turbine performance: (a) Surge motion. (b) Pitch motion. (c) Nacelle Velocity. (d) Nacelle Acceleration. SD: standard deviation.

In the previous figures, we only showed mean values and standard deviations for both models. To determine the integrity of the derived designs, it is also important to investigate the peak values that occur during the operational load cases listed in Table 11. As expected, the maximum values of the motions and nacelle velocities of the swivel model are close or smaller than those of the hinged model. These results again indicate the advantages of the swivel model over the hinged model.

Table 11. Peak values of swivel and reference model.

Parameters	Swivel Model		Hinged Model	
	Case 3	Case 10	Case 3	Case 10
Operational Load Cases	Case 3	Case 10	Case 3	Case 10
Max. Surge Displacement (m)	21.36	17.58	20.62	17.33
Max. Pitch Displacement (deg)	6.22	5.10	7.71	8.73
Max. Tower fore-aft Motion (m)	0.75	0.88	1.09	1.27
Max. Tower side-to-side Motion (m)	−0.014	0.012	−0.009	0.036
Max. Nacelle Velocity (m/sec)	3.19	4.16	3.97	7.09
Max. Nacelle Acceleration (m/sec ²)	1.66	2.79	2.84	4.28
Max. Tether Tension (kN)	2.19 × 10 ⁴	2.13 × 10 ⁴	2.35 × 10 ⁴	2.37 × 10 ⁴

4.4. Effect of Water Depth

Since the SWAY system is a FOWT for deepwater offshore locations in 100–400 m water depths, we model and examine two more cases with 100 m and 300 m water depths, to explore the platform response, as well as the wind turbine performance in different water depths. Figures 16 and 17 present the platform surge, pitch displacements, and the nacelle accelerations with 100 m and 300 m water depths. For comparison, we also list the standard deviation results for 100 m, 200 m, and 300 m water depth in Table 12.

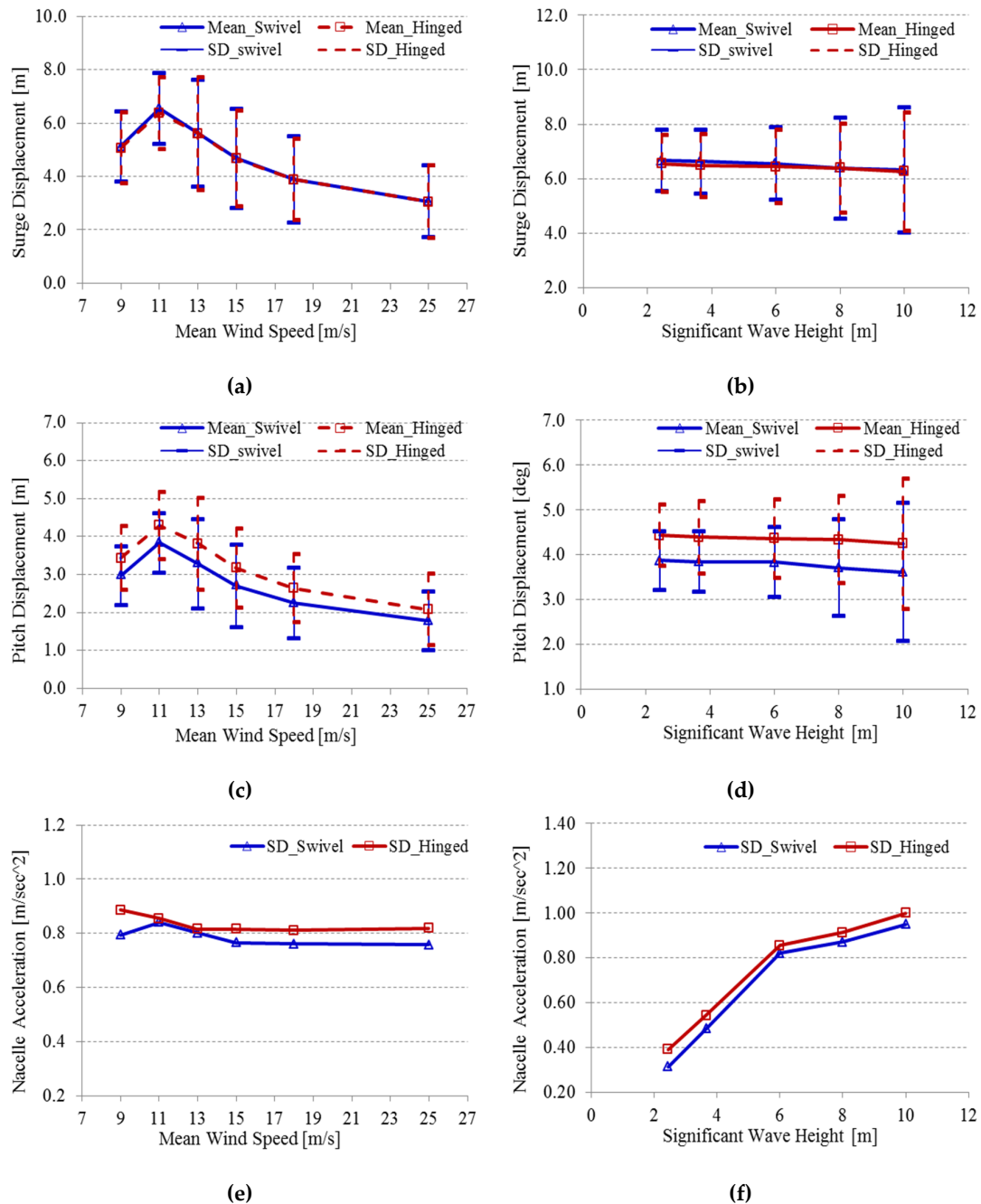
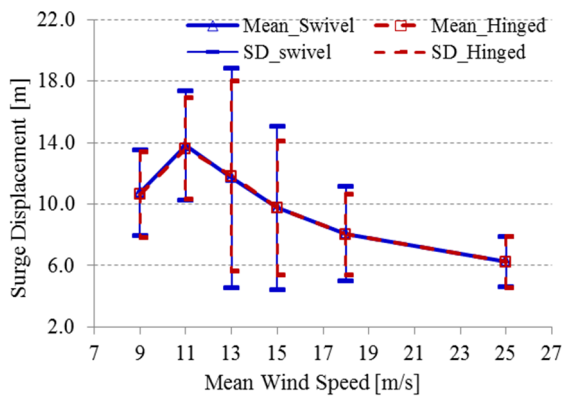
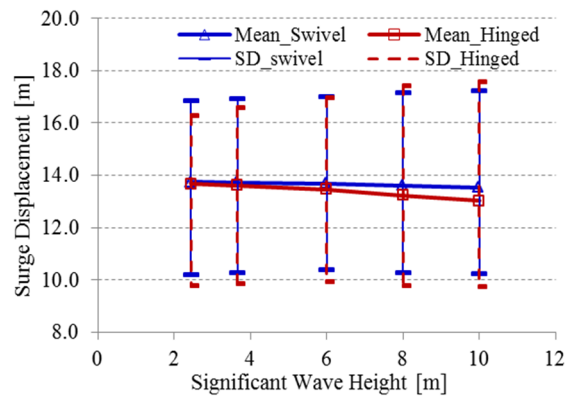


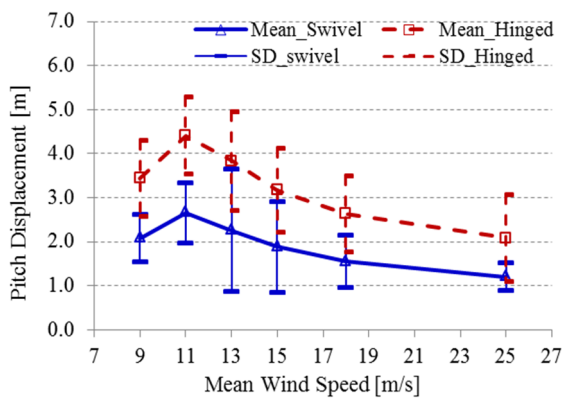
Figure 16. Surge/pitch motions and turbine performance with 100m water depth: (a) Surge motion V.S. Wind speed. (b) Surge motion V.S. Significant wave height. (c) Pitch motion V.S. Wind speed. (d) Pitch motion V.S. Significant wave height. (e) Nacelle acceleration V.S. Wind speed. (f) Nacelle acceleration V.S. Significant wave height. SD: standard deviation.



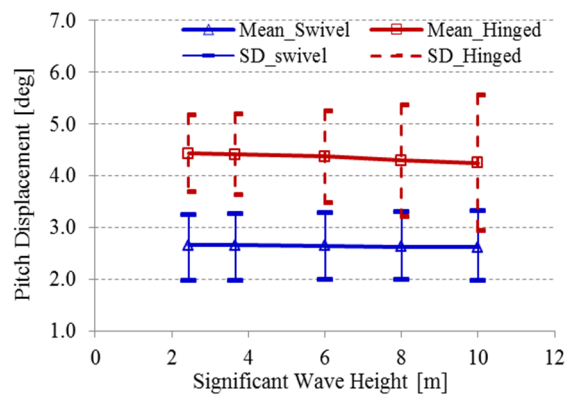
(a)



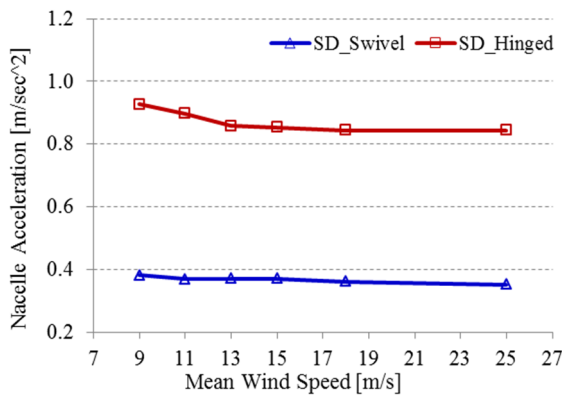
(b)



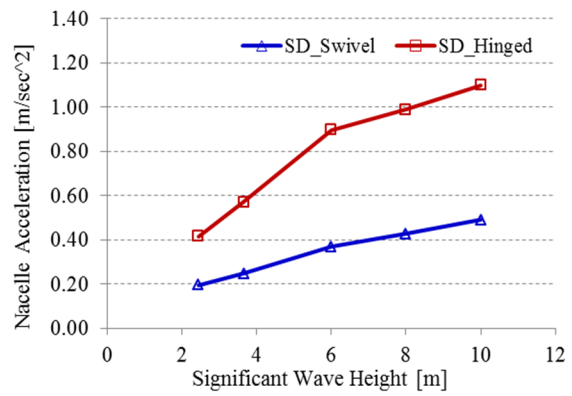
(c)



(d)



(e)



(f)

Figure 17. Surge/pitch motions and turbine performance with 300m water depth: (a) Surge motion V.S. Wind speed. (b) Surge motion V.S. Significant wave height. (c) Pitch motion V.S. Wind speed. (d) Pitch motion V.S. Significant wave height. (e) Nacelle acceleration V.S. Wind speed. (f) Nacelle acceleration V.S. Significant wave height. SD: standard deviation.

Table 12. Standard deviations of the SWAY model for various water depths ($U_{\text{mean}} = 11.4$ m/s).

Wave Condition		Surge (m)			Pitch (deg)			Nacelle Acceleration (m/sec ²)		
H _s (m)	T _p (s)	100m	200m	300m	100m	200m	300m	100m	200m	300m
2.4	8.1	1.1	2.4	3.3	0.7	0.7	0.6	0.3	0.3	0.2
3.7	9.7	1.2	2.4	3.3	0.7	0.7	0.6	0.5	0.4	0.3
6	10	1.3	2.2	3.3	0.8	0.7	0.6	0.8	0.5	0.4
8	12.5	1.9	2.3	3.4	1.1	0.7	0.7	0.9	0.6	0.4
10	14	2.3	2.6	3.5	1.5	0.8	0.7	0.9	0.6	0.5

From the comparison, we find that the surge motion increased with increasing water depth, while the pitch motion and the nacelle accelerations decreased in deeper water. We show that the nacelle accelerations in 300 m water depth are below the 0.5 m/sec² with various significant wave heights. In the cases with 100 m and 300 m water depth, the maximum allowable surge displacements are 8.75 m and 26.25 m, respectively, which satisfy the requirements discussed in the previous sections. We observe that the surge has not exceeded the maximum allowable surge motion in 300 m water depth under all operational load cases. All these results prove that the optimized SWAY model is a good candidate for deepwater development.

4.5. Fatigue States of the Sway Model

In practice, the fatigue and ultimate limit states are also important for the offshore wind turbine design [38,39]. The wind and wave effects on the wind turbine will generate damage to the structure. As a result, it would be important to check the fatigue life of the wind turbine due to different wind and wave conditions. Here, we further examine the fatigue state of the SWAY offshore turbine. We calculate the fatigue rate of the wind turbine tower for different wind and wave conditions, using the S-N method to evaluate the damage rate. By meeting the local minima with local maxima, we decompose the time series of the external loads into several cycles. The method assumes that the damage is accumulated linearly with each cycle i according to the Miner's rule. The damage rate is expressed as

$$DR = \sum_i \frac{n_i}{N_i(L_i^{RF})} / T, \quad (17)$$

$$N_i(L_i^{RF}) = \left(2 \frac{L^{ult} - |L^{MF}|}{L_i^{RF}} \right)^m \quad (18)$$

where n_i is the damage cycle, L_i^{RF} is the load range, L^{MF} is the mean of the load, L^{ult} is the ultimate load, which is selected to be 680,000 KNm for the tower base bending moment. The selection of m is based on DNV design standard and previous studies [38,40]. Based on Equations (17) and (18), we calculate and present the fatigue damage rate of the tower base fore-aft bending moment for different cases in Figure 18. We compared the different fatigues rate of the wind turbine tower for swivel and hinged connections. From the comparison, we observed that the fatigue rates of swivel connections are much lower than those of hinged connections, due to the large acceleration and velocity of the nacelle shown in Sections 4.1–4.3. As a result, we conclude that the use of the swivel connection can enhance the dynamics performance and the fatigue life of the offshore wind turbine. To investigate the fatigue damage rate's dependence on the environmental conditions, we compare the fatigue rate of the wind turbine tower for various significant wave heights H_s in Table 13. As expected, we found that significant wave heights have a negative effect on the fatigue rate.

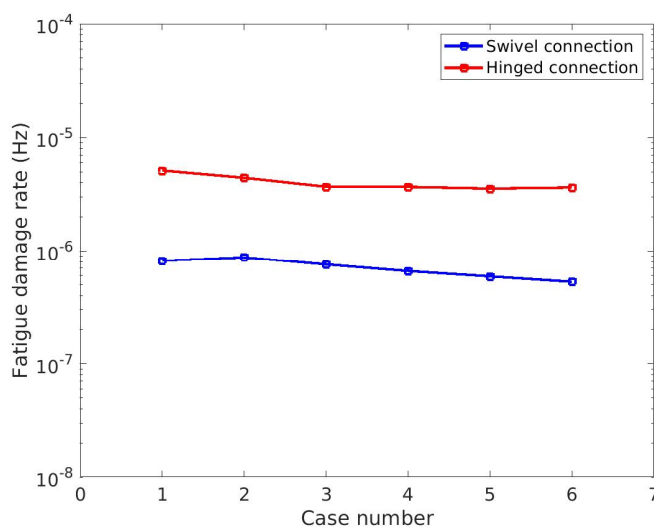


Figure 18. Fatigue damage rate (Hz) for different cases.

Table 13. Sensitivity of tower fatigue damage rater to significant wave height (H_s).

H_s (m)	3.66	8	10
Hinged connection DR (Hz)	6.6×10^{-7}	6.4×10^{-6}	9.7×10^{-7}
Swivel connection DR (Hz)	2.4×10^{-7}	1.5×10^{-6}	2.4×10^{-6}

5. Conclusions

The present study focuses on the design and dynamic analysis of the SWAY-concept FOWT. We first focus on the design optimization of the SWAY-concept FOWT. We present and analyze the most critical optimization criteria, including static, dynamics, and cost criteria. Through the iterative design process based on the above criteria, we obtain the optimal SWAY-concept FOWT. These procedures and the optimized model are of scientific and practical importance for the research and design optimization of the SWAY-concept or similar types of FOWTs.

We then demonstrate the dynamic performances of the optimal SWAY-concept FOWT. The SWAY model is established and simulated under different sea conditions by a fully coupled time-domain aero-hydro-servo-elastic model in FAST. An indoor program, HydroGen, calculates the hydrodynamics coefficients and forces on the supported platform. We focus on the swivel design at the subsea connection of the SWAY-concept FOWT, which is a unique feature of the SWAY model. To achieve this goal, we compare the dynamic performance between the optimized SWAY model and a reference model, with a hinged connection at the subsea connection between the platform and tether. Both swivel and hinged connections allow the tower system to rotate freely in the yaw mode. However, the swivel connection differs from the hinged connection for its additional restriction on the rotational motions. Thus, the swivel connection increases the stability of the offshore wind turbine and reduces the wind turbine structure’s damage rate. The peak values and standard deviation of structure displacements, nacelle velocity, and nacelle acceleration under different environmental conditions are calculated and compared. We also compared the fatigue life of the offshore wind turbine towers with swivel and hinged connections. From the comparisons, we find that the SWAY swivel model has better dynamics and stability performance when compared with the reference hinged model. The most significant discrepancy quantities between the dynamics performance of the swivel and hinged connection are the nacelle velocity and acceleration. For large wave conditions, the velocity and acceleration of the swivel connection cases are nearly twice as small as those of the hinged connection. Similarly, the fatigue damage rates of the turbine tower with swivel connection are lower than those of hinged connection for different load conditions. We also find that the tether of the present SWAY model did not undergo a loss of tension or exceed the maximum allowable tension under extreme conditions. We thus prove

that the present SWAY-concept FOWT design with the swivel connection is an excellent choice for deepwater deployment.

Author Contributions: Conceptualization, J.C.; methodology, J.C.; software and simulation, J.C. and C.L.; writing—original draft preparation, J.C.; writing—review and editing, C.L. All authors have read and agreed to the published version of the manuscript.

Funding: This research was partially supported by the American Bureau of Shipping scholarship program.

Conflicts of Interest: The authors declare no conflict of interest.

References

1. Sclavounos, P.; Tracy, C.; Lee, S. Floating offshore wind turbines: Responses in a seastate pareto optimal designs and economic assessment. In Proceedings of the International Conference on Offshore Mechanics and Arctic Engineering, Estoril, Portugal, 15–20 June 2008; Volume 48234, pp. 31–41.
2. Wang, C.; Utsunomiya, T.; Wee, S.; Choo, Y. Research on floating wind turbines: A literature survey. *IES J. Part A Civ. Struct. Eng.* **2010**, *3*, 267–277. [[CrossRef](#)]
3. Wu, X.; Hu, Y.; Li, Y.; Yang, J.; Duan, L.; Wang, T.; Adcock, T.; Jiang, Z.; Gao, Z.; Lin, Z.; et al. Foundations of offshore wind turbines: A review. *Renew. Sustain. Energy Rev.* **2019**, *104*, 379–393. [[CrossRef](#)]
4. Wayman, E.N. Coupled Dynamics and Economic Analysis of Floating Wind Turbine Systems. Ph.D. Thesis, Massachusetts Institute of Technology, Cambridge, MA, USA, 2006.
5. Crozier, A. Design and Dynamic Modeling of the Support Structure for a 10 MW Offshore Wind Turbine. Master's Thesis, Institutt for Energi-og Prosessteknikk, Kolbjørn, Hejes, 2011.
6. Bangga, G.; Lutz, T.; Jost, E.; Krämer, E. CFD studies on rotational augmentation at the inboard sections of a 10 MW wind turbine rotor. *J. Renew. Sustain. Energy* **2017**, *9*, 023304. [[CrossRef](#)]
7. Jonkman, J. *Definition of the Floating System for Phase IV of OC3*; National Renewable Energy Lab.(NREL): Golden, CO, USA, 2010.
8. Vesel, R.W., Jr.; McNamara, J.J. Performance enhancement and load reduction of a 5 MW wind turbine blade. *Renew. Energy* **2014**, *66*, 391–401. [[CrossRef](#)]
9. Dose, B.; Rahimi, H.; Herráez, I.; Stoevesandt, B.; Peinke, J. Fluid-structure coupled computations of the NREL 5 MW wind turbine by means of CFD. *Renew. Energy* **2018**, *129*, 591–605. [[CrossRef](#)]
10. Zhou, Y.; Xiao, Q.; Liu, Y.; Incecik, A.; Peyrard, C.; Li, S.; Pan, G. Numerical modelling of dynamic responses of a floating offshore wind turbine subject to focused waves. *Energies* **2019**, *12*, 3482. [[CrossRef](#)]
11. TC88-MT, IEC. *Iec 61400-3: Wind Turbines-Part 1: Design Requirements*; IEC: Geneva, Switzerland, 2005; Volume 64, pp. 1–85.
12. Jonkman, J.M. Dynamics of offshore floating wind turbines—Model development and verification. *Wind Energy Int. J. Prog. Appl. Wind Power Convers. Technol.* **2009**, *12*, 459–492. [[CrossRef](#)]
13. Nematbakhsh, A.; Olinger, D.J.; Tryggvason, G. Nonlinear simulation of a spar buoy floating wind turbine under extreme ocean conditions. *J. Renew. Sustain. Energy* **2014**, *6*, 033121. [[CrossRef](#)]
14. Hong, S.; Lee, I.; Park, S.H.; Lee, C.; Chun, H.-H.; Lim, H.C. An experimental study of the effect of mooring systems on the dynamics of a SPAR buoy-type floating offshore wind turbine. *Int. J. Nav. Archit. Ocean Eng.* **2015**, *7*, 559–579. [[CrossRef](#)]
15. Leimeister, M.; Kolios, A.; Collu, M.; Thomas, P. Design optimization of the OC3 phase IV floating spar-buoy, based on global limit states. *Ocean Eng.* **2020**, *202*, 107186. [[CrossRef](#)]
16. Jonkman, J.; Butterfield, S.; Musial, W.; Scott, G. *Definition of a 5-MW Reference Wind Turbine for Offshore System Development*; National Renewable Energy Lab.(NREL): Golden, CO, USA, 2009.
17. Hu, Y.; Wang, J.; Chen, M.Z.; Li, Z.; Sun, Y. Load mitigation for a barge-type floating offshore wind turbine via inerter-based passive structural control. *Eng. Struct.* **2018**, *177*, 198–209. [[CrossRef](#)]
18. He, E.-M.; Hu, Y.-Q.; Zhang, Y. Optimization design of tuned mass damper for vibration suppression of a barge-type offshore floating wind turbine. *Proc. Inst. Mech. Eng. Part M J. Eng. Marit. Environ.* **2017**, *231*, 302–315. [[CrossRef](#)]
19. Matha, D. *Model Development and Loads Analysis of an Offshore Wind Turbine on a Tension Leg Platform with a Comparison to Other Floating Turbine Concepts: April 2009*; National Renewable Energy Lab.(NREL): Golden, CO, USA, 2010.

20. Henderson, A.R.; Argyriadis, K.; Nichos, J.; Langston, D. Offshore wind turbines on TLPs—assessment of floating support structures for offshore wind farms in German waters. In Proceedings of the 10th German Wind Energy Conference, Bremen, Germany, 9 November 2010.
21. Moon, W.L., III; Nordstrom, C.J. Others tension leg platform turbine: A unique integration of mature technologies. In Proceedings of the SNAME 16th Offshore Symposium, The Society of Naval Architects and Marine Engineers, Houston, TX, USA, 9 February 2010.
22. Li, Y.; Tang, Y.; Zhu, Q.; Qu, X.; Wang, B.; Zhang, R. Effects of second-order wave forces and aerodynamic forces on dynamic responses of a TLP-type floating offshore wind turbine considering the set-down motion. *J. Renew. Sustain. Energy* **2017**, *9*, 063302. [[CrossRef](#)]
23. Casale, C.; Lembo, E.; Serri, L.; Viani, S. Preliminary design of a floating wind turbine support structure and relevant system cost assessment. *Wind Eng.* **2010**, *34*, 29–50. [[CrossRef](#)]
24. Bachynski, E.E.; Moan, T. Design considerations for tension leg platform wind turbines. *Mar. Struct.* **2012**, *29*, 89–114. [[CrossRef](#)]
25. Stewart, G.; Lackner, M.; Robertson, A.; Jonkman, J.; Goupee, A. *Calibration and Validation of a FAST Floating Wind Turbine Model of the DeepCwind Scaled Tension-leg Platform*; National Renewable Energy Lab.(NREL): Golden, CO, USA, 2012.
26. Meng, X.; Liu, X.; Tian, H.; Liu, M.; Wu, C. Optimal design and experimental evaluation of a TLP for FOWT at moderate water depth. In Proceedings of the The 26th International Ocean and Polar Engineering Conference, International Society of Offshore and Polar Engineers, Rhodes, Greece, 2–26 June 2016.
27. Song, J.; Lim, H.-C. Study of floating wind turbine with modified tension leg platform placed in regular waves. *Energies* **2019**, *12*, 703. [[CrossRef](#)]
28. Cermelli, C.; Aubault, A.; Roddier, D.; McCoy, T. Qualification of a semi-submersible floating foundation for multi-megawatt wind turbines. In Proceedings of the Offshore Technology Conference, Offshore Technology Conference, Houston, TX, USA, 3–6 May 2010.
29. Hall, M.; Goupee, A. Validation of a lumped-mass mooring line model with DeepCwind semisubmersible model test data. *Ocean Eng.* **2015**, *104*, 590–603. [[CrossRef](#)]
30. Uzunoglu, E.; Karmakar, D.; Soares, C.G. *Floating Offshore Wind Farms*; Springer: Berlin/Heidelberg, Germany, 2016; pp. 53–76.
31. Koh, J.; Ng, E.; Robertson, A.; Jonkman, J.; Driscoll, F. *Validation of a FAST Model of the SWAY Prototype Floating Wind Turbine*; National Renewable Energy Lab.(NREL): Golden, CO, USA, 2016.
32. Chen, J. Coupled Dynamic Analysis of Large-Scale Mono-Column Offshore Wind Turbine with a Single Tether Hinged in Seabed. Ph.D. Thesis, Texas A & M University, College Station, TX, USA, 2012.
33. Manwell, J.F.; McGowan, J.G.; Rogers, A.L. *Wind Energy Explained: Theory, Design and Application*; John Wiley & Sons: Hoboken, NJ, USA, 2010.
34. Shin, H.; Dam, P.T.; Jung, K.J.; Song, J.; Rim, C.; Chung, T. Model test of the OC3-Hywind floating offshore wind turbine. In Proceedings of the The Twenty-first International Offshore and Polar Engineering Conference, International Society of Offshore and Polar Engineers, Maui, HI, USA, 19–24 June 2011.
35. Cummins, W. *The Impulse Response Function and Ship Motions*; David Taylor Model Basin: Washington DC, USA, 1 October 1962.
36. Lee, C.-H. *WAMIT Theory Manual*; Department of Ocean Engineering, Massachusetts Institute of Technology: Cambridge, MA, UAS, 2 October 1995.
37. WITHEE, J.E. Fully Coupled Dynamic Analysis of a Floating Wind Turbine System. Ph.D. Thesis, Department of Ocean Engineering, Massachusetts Institution of Technology, Cambridge, MA, USA, 2004.
38. Li, L.; Cheng, Z.; Yuan, Z.; Gao, Y. Short-term extreme response and fatigue damage of an integrated offshore renewable energy system. *Renew. Energy* **2018**, *126*, 617–629. [[CrossRef](#)]
39. Li, L.; Yuan, Z.-M.; Gao, Y.; Zhang, X.; Tezdogan, T. Investigation on long-term extreme response of an integrated offshore renewable energy device with a modified environmental contour method. *Renew. Energy* **2019**, *132*, 33–42. [[CrossRef](#)]
40. Veritas, D.N. *Fatigue Design of Offshore Steel Structures*; DNV: Høvik, Norway, 2010; pp. 1–142.

